Screening plasmonic materials using pyramidal gratings

Hanwei Gao[a], Joel Henzie[b], Min Hyung Lee[b], and Teri W. Odom[a,b,1]

Departments of [a]Materials Science and Engineering and [b]Chemistry, Northwestern University, Evanston, IL 60208

Edited by George C. Schatz, Northwestern University, Evanston, IL, and approved October 28, 2008 (received for review September 10, 2008)

Surface plasmon polaritons (SPPs) are responsible for exotic optical phenomena, including negative refraction, surface enhanced Raman scattering, and nanoscale focusing of light. Although many materials support SPPs, the choice of metal for most applications has been based on traditional plasmonic materials (Ag, Au) because there have been no side-by-side comparisons of the different materials on well-defined, nanostructured surfaces. Here, we report a platform that not only enabled rapid screening of a wide range of metals under different excitation conditions and dielectric environments, but also identified new and unexpected materials for biosensing applications. Nanopyramidal gratings were used to generate plasmon dispersion diagrams for Al, Ag, Au, Cu, and Pd. Surprisingly, the SPP coupling efficiencies of Cu and Al exceeded widely used plasmonic materials under certain excitation conditions. Furthermore, grazing angle excitation led to the highest refractive index sensitivities (figure of merit >85) reported at optical frequencies because of extremely narrow SPP resonances (full-width-at-half-minimum <6 nm or 7 meV). Finally, our screening process revealed that Ag, with the highest sensitivity, was not necessarily the preferred material for detecting molecules. We discovered that Au and even Pd, a weak plasmonic material, showed comparable index shifts on formation of a protein monolayer.

nanophotonics | surface plasmon polariton | dispersion diagrams | chemical and biological sensing

Surface plasmon polaritons (SPPs) are collective excitations of free electrons trapped at a metal/dielectric interface (1). In the form of SPPs, light can be manipulated at length scales exceeding the diffraction limit (2, 3), which has the potential to transform chemical and biological sensing (4–7), imaging (8–10), and optoelectronics (11–13). To accelerate progress in any area; however, it is critical that rational design play an increasingly important role in developing standards so that applications based on SPP-supporting materials are not selected based on history or availability, but because of their optimal properties. For example, the grand challenge in SPP-based sensing is to achieve single (bio)molecule selectivity and sensitivity, but there are few reports on how to optimize the geometry of the nanostructures or their materials composition for a wide range of chemical environments. Recent reviews on different sensing modalities have also only explored a limited number of plasmonic materials and without seriously considering excitation conditions (14–16). Moreover, nontraditional plasmonic materials such as Cu and Al are desirable for electronic device applications, and catalytically active metals, including Pd (17) [and Cu (18)], are useful in monitoring surface reactions.

The frequency range over which SPP resonances exist is dominated by intrinsic materials properties. Specifically, interband transitions of the metal play a large role in determining the relative electric permittivity (ε_m), which sets an upper limit on the energy of surface plasmons. In order of decreasing energy, Al, Pd, Ag, Au, and Cu have interband transitions from the deep UV to the red-end of the visible spectrum (19–21). Because of the momentum mismatch between surface plasmons and photons (22, 23), different mechanisms have been pursued to excite SPPs on metal films (1, 24). For a 2D grating, SPPs Bloch wave modes are generated under the Bragg coupling condition (25):

$$\frac{\omega}{c}\sqrt{\frac{\varepsilon_m\varepsilon_d}{\varepsilon_m+\varepsilon_d}} = |\boldsymbol{k}_0 \sin\theta + i\boldsymbol{G}_x + j\boldsymbol{G}_y| \qquad [1]$$

where ω, c, and k_0 are the angular frequency, speed, and momentum of free-space light. ε_d is the relative permittivity of the adjacent dielectric, which can be expressed in terms of refractive index ($n = \sqrt{\varepsilon_d}$) for nonabsorptive materials. Thus, SPP Bloch wave modes characterized by the integer pair of indices (i, j) can be formed at specific angles of incidence θ. Accordingly, the magnitudes of the Bragg vectors for a square grating are $|\boldsymbol{G}_x| = |\boldsymbol{G}_y| = 2\pi/a_0$, where the grating pitch a_0 defines the size of the first Brillouin zone. Each of these variables can be tuned to expand the range of possible plasmonic behavior.

Here, we present a platform to screen plasmonic materials by independently controlling: (*i*) the material, (*ii*) the surface geometry, (*iii*) the dielectric environment, and (*iv*) the excitation angle. The key, enabling factor of this approach is the wafer-scale patterning of 2D nanopyramidal grating arrays. Although micropyramidal arrays coated with an Au layer have been shown to support SPPs, the angle-resolved spectral features were not well-defined and in poor agreement with calculations; one reason is that both pyramid size and pitch had microscale dimensions (26). Our subwavelength gratings supported characteristic SPP resonances across optical frequencies that made possible a side-by-side comparison of dispersion diagrams of 5 different metals (Al, Ag, Au, Cu, and Pd) out to large wavevectors (angles up to 70°). We discovered that the high-order SPP Bloch wave modes of Au and Cu were similar and observed the demonstration of surface plasmons on Pd gratings. In addition, we determined the SPP coupling efficiencies of the different metals, which can now be considered as a design parameter for plasmonic devices. Finally, we applied the outcomes of these screening experiments to 2 different problems: achieving high sensitivities on SPP grating sensors and testing whether these gratings could detect changes in the local dielectric environment, such as adsorption of protein (biotin-avidin) monolayers. Our nanopyramidal platform enabled us to find that materials with the highest sensitivities to bulk refractive indices were not necessarily the best for detecting molecules, and that relatively unexplored metals could produce sensing responses rivaling those of Au and Ag.

Platform for Tailoring SPP Resonances on Metal Gratings

Soft interference lithography was used to fabricate cm^2-areas of subwavelength metal gratings on Si (100) templates (Fig. 1*A*) (27, 28). The templates were patterned with 2D square arrays of pyramidal pits on a pitch a_0 = 400 nm with a pyramid base length

Author contributions: H.G. and T.W.O. designed research; H.G. and J.H. performed research; J.H. and M.H.L. contributed new reagents/analytic tools; H.G., J.H., and T.W.O. analyzed data; and H.G., J.H., M.H.L., and T.W.O. wrote the paper.

The authors declare no conflict of interest.

This article is a PNAS Direct Submission.

[1]To whom correspondence should be addressed. E-mail: todom@northwestern.edu.

This article contains supporting information online at www.pnas.org/cgi/content/full/0809034105/DCSupplemental.

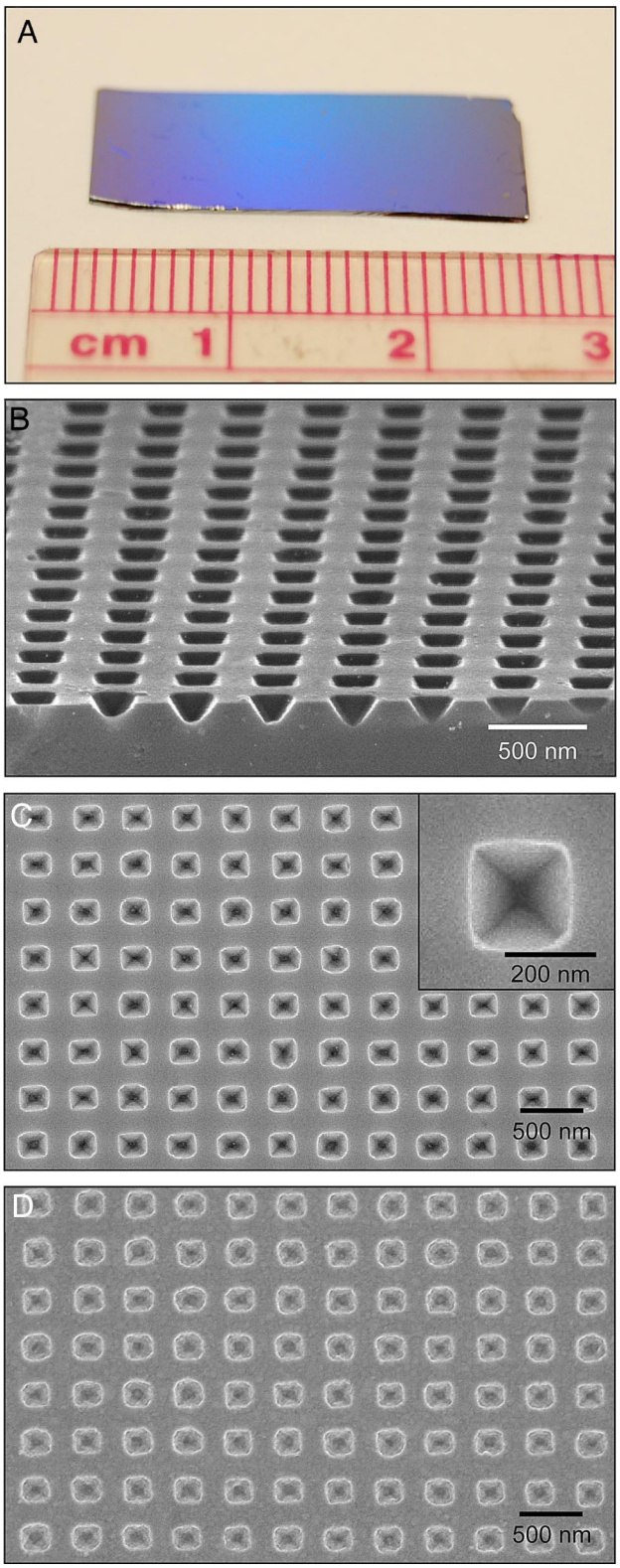

Fig. 1. Plasmonic materials on 2D nanopyramidal gratings. Optical micrograph (*A*) and scanning electron microscopy (SEM) (*B* and *C*) images of a large-area (0.9 cm × 2.3 cm) Si nanopyramidal grating. (*D*) SEM image of a 170-nm-thick Au film deposited on the Si template.

of 220 nm (Fig. 1 *B* and *C*). The size of the pyramid unit cell could be changed by adjusting the wet chemical etching time during the patterning of the template [see supporting information (SI) Fig. S1 *A–B*]. Different metals were deposited by e-beam directly onto the Si substrate without an adhesion layer, and the film thickness was fixed at 170 nm. The refractive index of the top surface (superstrate) was changed by using oils with different refractive indices (n = 1.29, 1.52, 1.65). Fig. 1*D* depicts a top-down view of a typical Au nanopyramidal grating.

Angle-resolved reflection spectra from the nanopyramidal gratings were acquired from θ = 6–70° in steps of 1° by using p-polarized white light. We converted wavelength vs. angle data (see *Methods*) to photon energy vs. in-plane wavevector (k) data to construct dispersion diagrams; the grayscale level represents the reflection intensity. Fig. 2*A* depicts that Au gratings with a superstrate of air (n = 1) supported a distinct plasmon resonance (dip) that shifted to lower energies as the wavevector (or angle) increased. The overall trends of this mode were in good agreement with the simple dispersion relation predicted by Eq. **1** (red, dashed curve), indicating that the resonance originated from the $(-1,0)_{\text{Au-air}}$ SPP Bloch mode. A Wood's anomaly, which is a geometric effect corresponding to light diffracted at an angle parallel to the metal surface (29), is represented by the blue, dashed line. Higher-order modes could not be distinguished from the interband transition of Au (≈2.5 eV) (19, 20) but could be observed by increasing the index of the superstrate (Fig. 2 *B* and *C*).

Deviation between experimental and theoretical curves at low angles of incidence is expected because of the formation of plasmonic band gaps as k approaches zero (30–32). This difference is clearly illustrated in Fig. 2*C*, where an experimental band gap centered ≈1.8 eV appeared between $(-1,0)_{\text{Au-oil}}$ and $(+1,0)_{\text{Au-oil}}$ bands at small k. Other calculations have indicated that the amount of band-bending and the magnitude of the band gap depends on the size and shape of the unit cell (22). Our results on Au gratings patterned with larger pyramids (base length, 320 nm) agree with these predictions (Fig. S1 *C–D*). Although Au nanopyramidal gratings exhibited SPP modes that were tunable over a relatively wide energy range (in air, 1.58–2.35 eV), SPP resonances that occur at higher and lower energies are often desirable. Thus, we fabricated Ag, Al, and Pd gratings to investigate SPP behavior in the UV to visible range and Cu gratings from visible to near-infrared by using the same template.

Because the interband transition for Ag occurs at 3.8 eV (19, 20), $(-1,0)_{\text{Ag-air}}$ resonances at energies of 2.48 eV could be observed even at low angles (Fig. 2*D*). Fig. 2 *E* and *F* indicates that the higher-order modes in Ag were strikingly different from the ones in Au with superstrates n = 1.29 and 1.52: the slopes of the bands were steeper, and the bands were not as compressed at energies >2.3 eV. Fig. 3 *A* and *B* shows that Al nanopyramidal gratings supported (−1, 0) modes that were blue-shifted compared with those on Ag and Au gratings. Because the interband transition of Al is in the deep UV, higher-order modes such as $(+1, \pm1)_{\text{Al-oil}}$ could be resolved at high (3.0 eV) energies. The widths of these bands were broadened, however, which indicated less coherent coupling. Moreover, we examined nanopyramidal gratings made of Pd, a less efficient plasmonic material (33) compared with Ag and Al because of its relatively large imaginary component of ε_m. Surprisingly, we discovered that Pd gratings supported SPP waves at visible wavelengths with well-defined dispersion curves that were in agreement with calculated SPP Bloch wave modes (Fig. 3 *C* and *D*).

For the case of Cu nanopyramidal gratings, no well-defined SPP resonances were found at low-incident angles when n = 1 (Fig. 3*E*) because of the interband transition at 2.1 eV (21, 34, 35). A pronounced $(-1,0)_{\text{Cu-air}}$ mode only appeared at angles greater than θ = 22°. The same (−1,0) SPP Bloch wave mode could also be revealed by increasing the superstrate n (Fig. 3*F*). For example, when n = 1.52, not only was the (−1,0) mode present, but higher modes such as (0, ±1), (+1,0), and (−1, ±1) were also observed. Besides the energy differences of the interband transitions of Au and Cu (2.5 eV vs. 2.1 eV), the overall features of the dispersion diagrams were similar: the plasmonic band gaps appeared at close

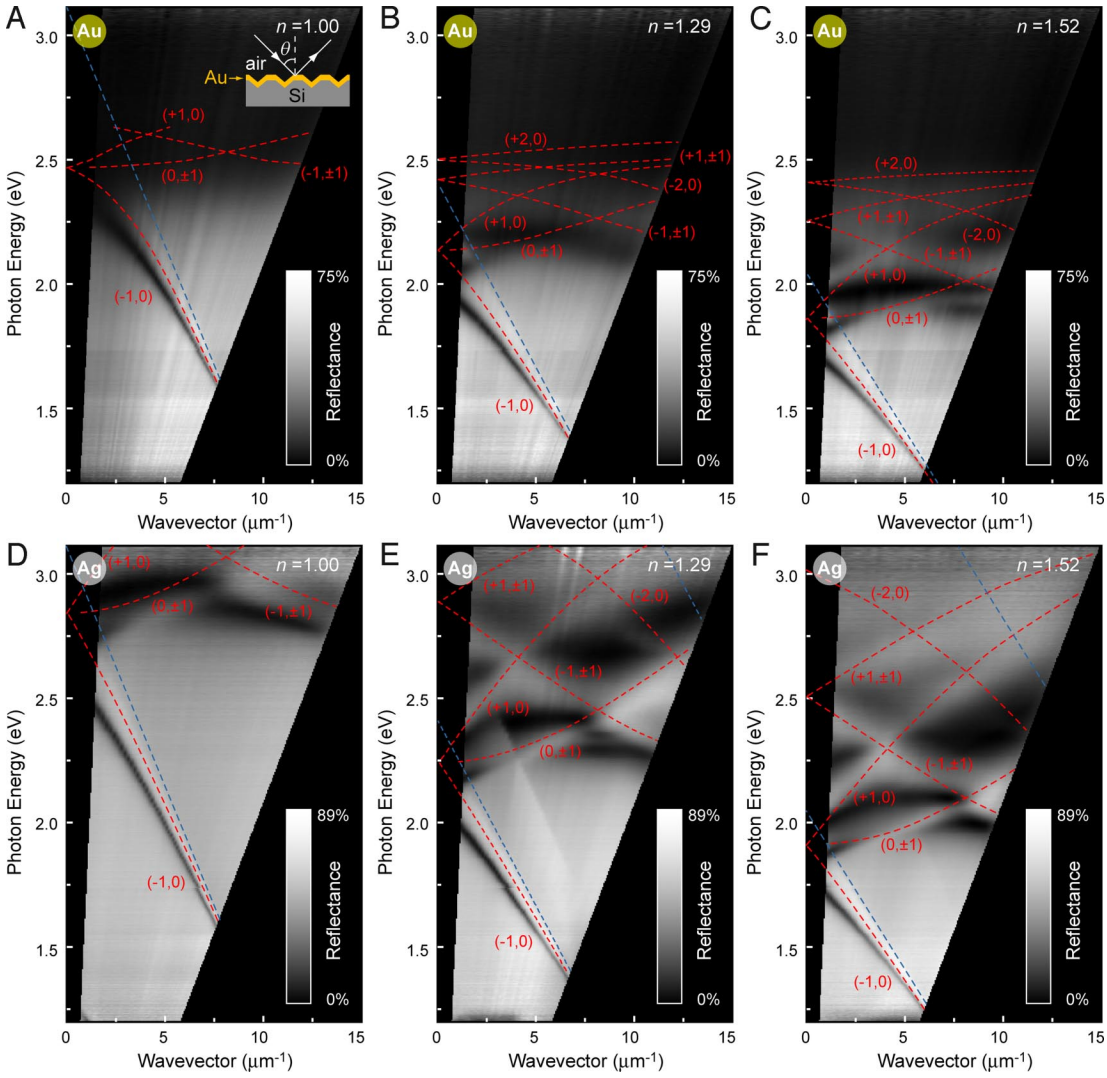

Fig. 2. Dispersion diagrams of Au and Ag nanopyramidal gratings. Measured reflection energy disperion as a function of in-plane wavevector on Au (*A–C*) and Ag (*D–F*) pyramidal gratings under *p*-polarized white light. Calculated SPP Bloch waves from Eq. **1** are denoted by dashed red lines, and dashed blue lines represent Wood's anomalies.

to the same energy, and the higher-order bands were flat. Such analogous behavior suggests that Cu could be a viable alternative to Au for applications that require cheaper materials and integration into electronic devices.

Importantly, we can quantify a SPP coupling efficiency (η) from the dispersion diagrams, which can be interpreted as the percentage of energy transferred from free-space photons to surface plasmons. We define this efficiency as the depth of the SPP resonance normalized by the reflection intensity of the baseline:

$$\eta = (I_{\text{base}} - I_{\text{min}})/I_{\text{base}} \qquad [2]$$

Fig. 4 compares η of all 5 metals at different excitation angles for each (−1,0)SPP mode in air. The trends for Au and Cu are similar: η is low at small θ because of interband transitions (where SPPs do not contribute much) and peaks at $\theta = 30°$. In contrast, η for Ag monotonically decreases as a function of angle, whereas η for Al stays nearly constant. At $\theta = 50°$, Al nanopyramidal gratings had SPP coupling efficiencies up to 68.0%, which is comparable to Ag (77.6%) at $\theta = 6°$ and Au (78.8%) at $\theta = 27°$. Moreover, at $\theta > 50°$, η for Al exceeded those for Ag, Au, and Cu. At our highest excitation angle ($\theta = 70°$), $\eta = 54.5\%$ for Al gratings, 49.1% for Cu, 41.7% for Ag, and 38.4% for Au. As expected, η for Pd (35%) was less than the other 4 metals.

High Refractive Index Sensitivity Under Grazing Angle Excitation

SPP resonance sensors based on subwavelength metal gratings are considerably more compact than those based on prisms (16) and are predicted to produce sensitivities comparable to those on prism couplers at grazing angles of incidence (36, 37). Although there are more sophisticated ways to evaluate the sensitivity of plasmonic sensors (24), a convenient metric is the figure of merit (FOM), which is defined as the shift in energy of the resonance per refractive index unit (RIU) divided by the FWHM of the resonance (38). From our screening procedure with bulk n superstrates, we found that Ag gratings exhibited larger FOM values than Au, Al, Cu, and Pd at all excitation angles (Table 1).

Fig. 5 highlights the sensing characteristics of Ag nanopyramidal gratings. There are several significant aspects of these data. First, at a low angle of $\theta = 13°$, the $(-1,0)_{\text{Ag}}$ SPP mode shifted from 535.3 nm ($n = 1$) to 805.3 nm ($n = 1.65$) (Fig. 5*A*), whereas at a grazing angle of $\theta = 64°$, the mode shifted from 775.0 nm ($n = 1$) to 985.8 nm ($n = 1.52$) (Fig. 5*B*). Thus, different excitation angles produced

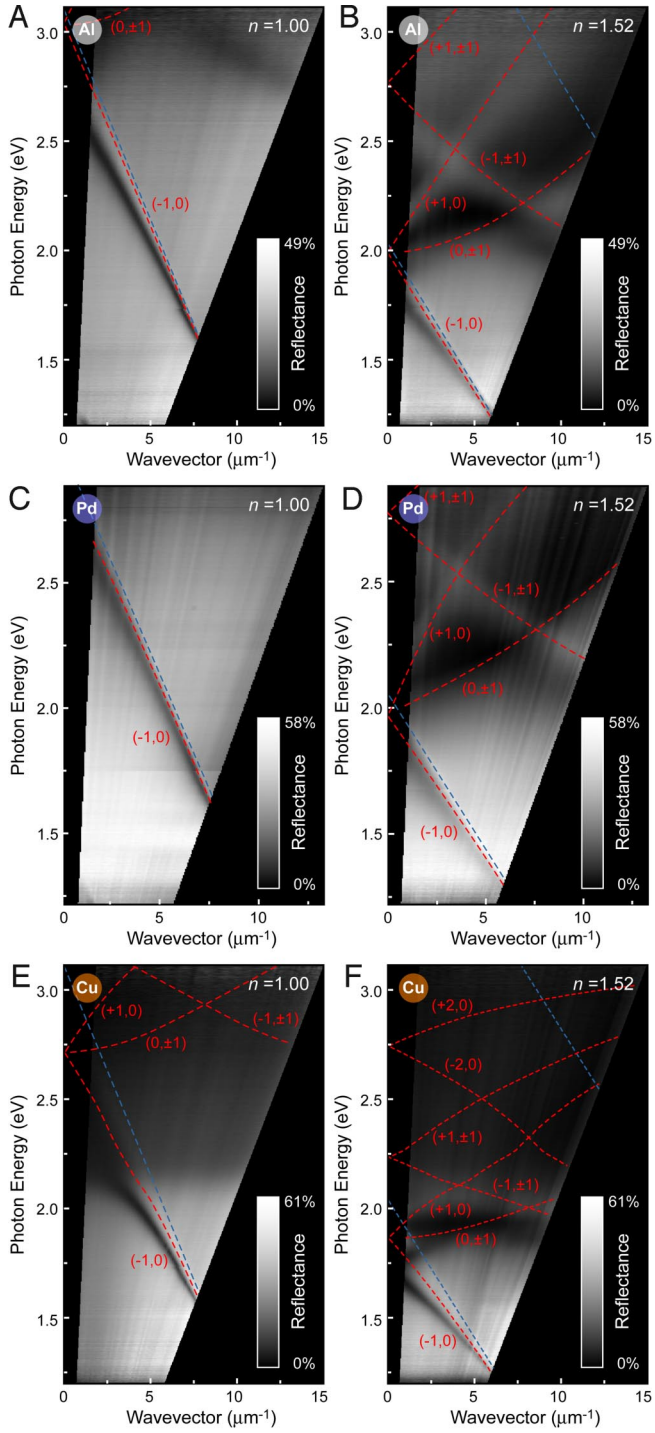

Fig. 3. Dispersion diagrams of Al, Pd, and Cu nanopyramidal gratings. Measured reflection energy disperion as a function of in-plane wavevector on Al (*A* and *B*), Pd (*C* and *D*), and Cu (*E* and *F*) pyramidal gratings under *p*-polarized white light. Calculated SPP Bloch waves are denoted by dashed red lines, and dashed blue lines represent Wood's anomalies.

the same slope of 410.4 ± 5.0 nm/RIU (Fig. 5*C*), which is the largest shift expected for gratings with pitch a_0 = 400 nm. Second, the plasmon resonance dips narrowed significantly at high excitation angles while maintaining a fairly high η (35.6%). This narrowing is most likely related to increased propagation distances of SPPs having longer wavelengths at high excitation angles, which would result in coherent coupling among more unit cells.

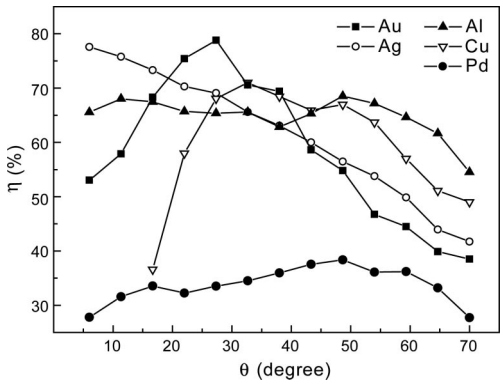

Fig. 4. SPP coupling efficiency of $(-1,0)_{\text{metal-air}}$ SPP Bloch waves at different excitation angles. Nanopyramidal gratings made of Au (■), Ag (○), Al (▲) Cu (▽) and Pd (●) exhibited high SPP coupling efficiencies. The coupling efficiencies for Au and Cu are reduced at lower angles because of interband transitions.

We calculated the FOM values by measuring the FWHM of the resonances under different n (Fig. 5*D*). At θ = 13°, the average FWHM of the dip was 13.6 nm (0.0378 eV), and the FOM was calculated to be 34.1 ± 3.6. At θ = 64°, the FWHM of the $(-1,0)_{\text{Ag}}$ SPP resonance was as narrow as 5.2 nm (0.0085 eV) for n = 1.52, which translated into an extremely high FOM of 85.1 ± 1.6. Furthermore, angle-dependent sensitivities were observed with the other metals (Fig. S2) and which also depended on the geometry of the unit cells. For example, at θ = 64°, $(-1,0)_{\text{Au-air}}$ SPP resonances had a FWHM of 7.1 nm for 220-nm pyramids; 12.8 nm for 320-nm pyramids; and 9.7 nm for 100-nm circular holes (27) (Fig. S3). Although gratings from these materials were slightly less sensitive to bulk n compared with Ag (Table 1), their FOMs under grazing angles were still at least 2–4 times higher than other sensing modalities (27, 39). Native oxide layers (often submonolayer) associated with Ag, Al, and Cu (40–42) are often a disadvantage when considering other materials for sensing. We found that for bulk n, the oxide did not greatly affect the plasmon resonances. Comparisons of spectra from a Cu nanopyramidal grating stored in air for 1 month and one of freshly deposited Cu showed <5% decrease in efficiency and SPP wavelengths shifts <1 nm.

Sensitivity of Pyramidal Gratings to Protein Monolayers

Because the nanopyramidal gratings exhibit SPP resonances with high signal-to-background ratios over a wide range of excitation angles, improved quantitative measurements with better accuracy and less uncertainty can be achieved for molecular sensing. We tested whether Ag, Au, and Pd nanopyramidal gratings were sensitive to local refractive index changes on binding of avidin to biotinylated metal surfaces. To prime the substrates, a monolayer of cystamine was first assembled onto freshly deposited metal gratings to avoid metal oxidation and to facilitate the assembly of a uniform layer of biotin (43). Fig. 6 displays how the (−1,0) resonances changed after assembling a layer of biotin and then binding a monolayer of avidin at the same low and high excitation angles as in Fig. 5. Fig. 6 *A* and *B* indicate that the Ag resonances were narrower than those of Au (Fig. 6 *C* and *D*) but that the absolute shifts in wavelength were approximately half when a

Table 1. FOMs of nanopyramidal gratings made from different metals and under different excitation angles

	Au	Ag	Al	Cu	Pd
θ = 13°	24.4	34.1	17.2	18.0	14.6
θ = 64°	67.0	85.1	30.2	32.9	24.3

CHEMISTRY

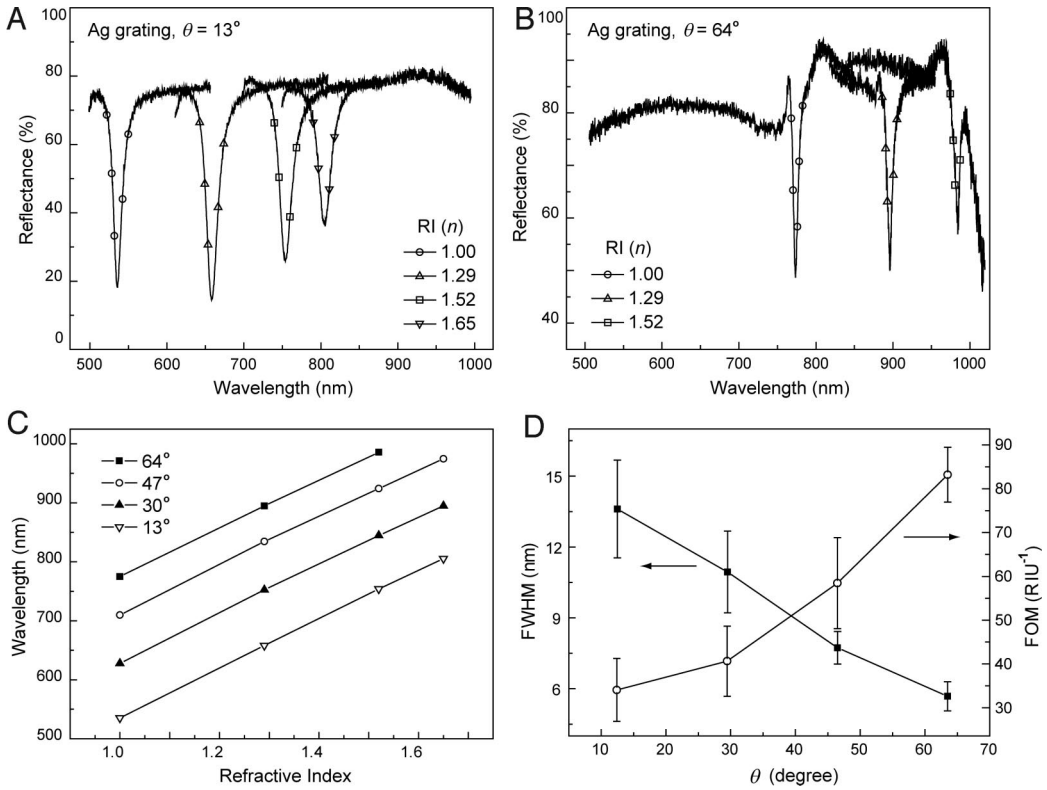

Fig. 5. Angle-dependent refractive index sensitivity on Ag pyramidal gratings. Reflection spectra measured on Ag nanopyramidal gratings at $\theta = 13°$ (*A*) and $\theta = 64°$ (*B*). (*C*) Large shifts (≈410 nm/RIU) of the $(-1,0)_{Ag}$ mode was observed at all angles. (*D*) FOM and FWHM of Ag gratings depended strongly on angle.

saturated layer of avidin was assembled on biotin. At $\theta = 13°$, Ag showed a resonance shift of 2.7 nm, whereas Au shifted by 5.0 nm, much larger than previous biotin-avidin reports (44, 45). Although the red-shifts at $\theta = 64°$ were somewhat less, the narrowness of the resonances at high angles made the shifts easier to quantify without needing to fit the data (46).

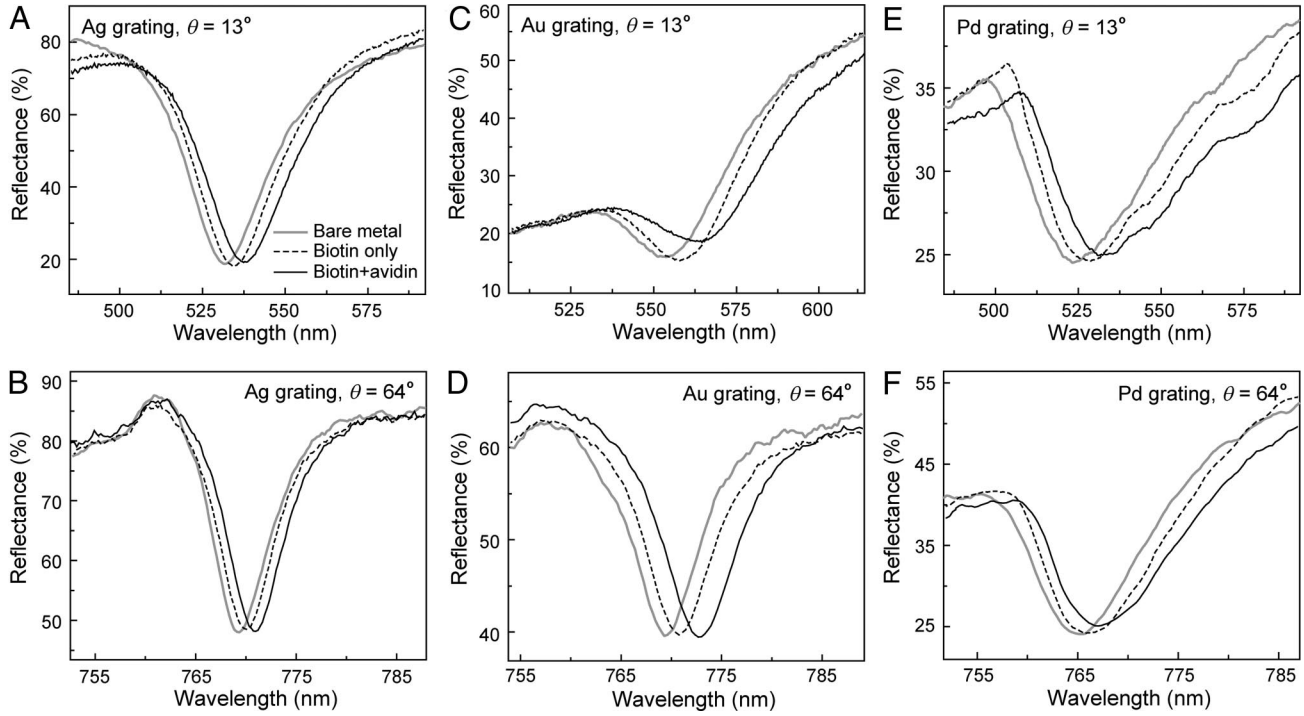

Fig. 6. Local refractive index sensing by using Ag, Au, and Pd pyramidal gratings. Reflection spectra at $\theta = 13°$ and $\theta = 64°$ for Ag (*A* and *B*), Au (*C* and *D*), and Pd (*E* and *F*) for the bare metal (gray curves), on assembly of a layer of biotin (dashed curves), and after binding a layer of avidin (black curves).

We also tested the molecular sensing characteristics of Pd gratings. Surprisingly, although the SPP coupling efficiency η was fairly weak, and the FOM for bulk n was also less than those of Ag and Au, the amount of the plasmon resonance shift on binding avidin (4.9 nm) was similar to Au and greater than that of Ag. Our discovery of Pd as a material for detecting protein–protein interactions by using a grating structure is significant. First, the relatively broad and asymmetric $(-1,0)$ Pd resonances did not obscure the large resonance shifts on formation of protein monolayers. Second, Pd does not oxidize easily and supports the formation of self-assembled monolayers (47). Third, SPP sensors based on free-space excitation of gratings provide a simpler and alternative approach to detect changes in the local environment. Finally, and perhaps most importantly, the success of Pd for measuring molecular monolayers paves the way for other nontraditional and less efficient plasmonic materials to be considered for current and emerging applications.

Methods

Fabrication. The grating template was fabricated by patterning 100-nm diameter photoresist posts (Shipley 1805) at a 400-nm pitch on a Si (100) wafer. A 20-nm-thick layer of Cr was deposited on the pattern by electron beam deposition, and then the photoresist was lifted off to reveal holes in Cr of the same diameter and pitch. These holes were used as a mask to anisotropically etch the underlying Si (100). Pyramidal pits were formed beneath the holes with 4 intersecting Si (111) faces. Different metals were deposited on this Si grating template to produce 2D nanopyramidal gratings.

Calculations. The angle-resolved reflection spectra were acquired as θ vs. λ, and then converted to ω (eV) vs. k_x (μm^{-1}) by using the following equations:

$$\hbar\omega = 1240/\lambda(\text{eV})$$

$$k_x = k_0 \cdot \sin\,\theta = 2\pi/\lambda \cdot \sin\,\theta(\mu\text{m}^{-1})$$

Such dispersion diagrams can then be directly compared with theoretical dispersion curves of SPP Bloch wave modes calculated by using Eq. **1**. ε_m values were taken from the literature values given by Johnson and Christy (20, 34) (Au, Cu, and Pd) and Palik (19) (Ag and Al).

Preparation of Substrates for Protein Assembly. The procedure for binding avidin to biotinylated surfaces was adapted from ref. 44. For our system, immediately after the metal was deposited on the etched Si templates, the gratings were immersed in a 0.1 M solution of cystamine (Sigma Aldrich) for 24 h to form a self-assembled monolayer. After many successive rinses with ethanol and deionized (DI) water, the nanopyramidal gratings were placed in a 20 mM solution of biotin (Sigma Aldrich) in dimethylformamide for 24 h. Again, the substrate was copiously rinsed with DI water before being immersed in a 10 μg/ml solution of ExtrAvidin (Sigma Aldrich E2511, dissolved in 10 mM PBS at pH 8.0) for 15 min. We found that this concentration and binding time produced a saturated coverage of avidin on the biotin layer. The sample was then cleaned up by rinsing with DI water and drying under nitrogen before the reflection spectra were measured.

ACKNOWLEDGMENTS. This work was supported by National Science Foundation Grant DMR-0705741, National Science Foundation-Nanoscale Science and Engineering Center Award EEC-0647560, and National Science Foundation-Materials Research Science and Engineering Center Grant DMR-0520513 at the Materials Research Center. This work was performed in the NU*ANCE* Center facilities, which are supported by National Science Foundation-Materials Research Science and Engineering Centers, National Science Foundation-Nanoscale Science and Engineering Center, and the Keck Foundation.

1. Raether H (1989) *Surface Plasmons* (Springer, Hamburg).
2. Maier SA, *et al.* (2001) Plasmonics: A route to nanoscale optical devices. *Adv Mater* 13:1501–1505.
3. Barnes WL, Dereux A, Ebbesen TW (2003) Surface plasmon subwavelength optics. *Nature* 424:824–830.
4. Ostuni E, Chapman RG, Holmlin RE, Takayama S, Whitesides GM (2001) A survey of structure-property relationships of surfaces that resist the adsorption of proteins. *Langmuir* 17:5605–5620.
5. Homola J (2003) Present and future of surface plasmon resonance biosensors. *Anal Bioanal Chem* 377:528–539.
6. Stewart ME, *et al.* (2006) Quantitative multispectral biosensing and 1d imaging using quasi-3d plasmonic crystals. *Proc Natl Acad Sci USA* 103:17143–17148.
7. Stewart ME, *et al.* (2008) Nanostructured plasmonic sensors. *Chem Rev* 108:494–521.
8. Pendry JB (2000) Negative refraction makes a perfect lens. *Phys Rev Lett* 85:3966–3969.
9. Shalaev VM (2007) Optical negative-index metamaterials. *Nat Photon* 1:41–48.
10. Zhang X, Liu Z (2008) Superlenses to overcome the diffraction limit. *Nat Mater* 7:435.
11. Bergman DJ, Stockman MI (2003) Surface plasmon amplification by stimulated emission of radiation: Quantum generation of coherent surface plasmons in nanosystems. *Phys Rev Lett* 90:027402.
12. Dickson W, Wurtz GA, Evans PR, Pollard RJ, Zayats AV (2008) Electronically-controlled surface plasmon dispersion and optical transmission through hole arrays in metal films with liquid crystal. *Nano Lett* 8:281–286.
13. Okamoto K, *et al.* (2004) Surface-plasmon-enhanced light emitters based on ingan quantum wells. *Nat Mater* 3:601.
14. Homola J (2006) *Surface Plasmon Resonance Based Sensors* (Springer, New York).
15. Sharma AK, Jha R, Gupta BD (2007) Fiber-optic sensors based on surface plasmon resonance: A comprehensive review. *IEEE Sens J* 7:1118–1129.
16. Kasunic KJ (2000) Comparison of kretschmann-raether angular regimes for measuring changes in bulk refractive index. *Appl Opt* 39:61–64.
17. Ka PT, Hugon O, Trouillet A, Gagnaire H (2001) An integrated optic hydrogen sensor based on spr on palladium. *Sens Actuators B* 74:168–172.
18. Williams SM, *et al.* (2004) Use of the extraordinary infrared transmission of metallic subwavelength arrays to study the catalyzed reaction of methanol to formaldehyde on copper oxide. *J Phys Chem B* 108:11833–11837.
19. Palik ED (1997) *Handbook of Optical Constants of Solids* (Academic, New York).
20. Johnson PB, Christy RW (1972) Optical constants of the noble metals. *Phys Rev B* 6:4370.
21. Lide DR (2008) *CRC Handbook of Chemistry and Physics* (CRC Press, Boca Raton, FL).
22. Giannattasio A, Hooper IR, Barnes WL (2006) Dependence on surface proÞle in grating-assisted coupling of light to surface plasmon-polaritons. *Opt Commun* 261:291–295.
23. Degiron A, Lezec HJ, Barnes WL, Ebbesen TW (2002) Effects of hole depth on enhanced light transmission through subwavelength hole arrays. *Appl Phys Lett* 81:4327.
24. Homola J, Koudela I, Yee SS (1999) Surface plasmon resonance sensors based on diffraction gratings and prism couplers: Sensitivity comparison. *Sens Actuators B* 54:16–24.
25. Barnes WL, *et al.* (2004) Surface plasmon polaritons and their role in the enhanced transmission of light through periodic arrays of sub-wavelength holes in a metal film. *Phys Rev Lett* 92:107401.
26. Perney NMB, Baumberg JJ (2006) Tuning localized plasmons in nanostructured substrates for suface-enhanced raman scattering. *Opt Express* 14:847–857.
27. Henzie J, Lee MH, Odom TW (2007) Multiscale patterning of plasmonic metamaterials. *Nat Nanotech* 2:549–554.
28. Henzie J, Kwak E-S, Odom TW (2005) Mesoscale metallic pyramids with nanoscale tips. *Nano Lett* 5:1199–1202.
29. Wood RW (1902) On a remarkable case of uneven distribution of light in a diffraction grating spectrum. *Phil Mag* 4:396–408.
30. Barnes WL, Preist TW, Kitson SC, Sambles JR (1996) Physical origin of photonic energy gaps in the propagation of surface plasmons on gratings. *Phys Rev B* 54:6227–6244.
31. Kitson SC, Barnes WL, Sambles JR (1996) Full photonic band gap for surface modes in the visible. *Phys Rev Lett* 77:2670–2673.
32. Kelf TA, Sugawara Y, Baumberg JJ (2005) Plasmonic band gaps and trapped plasmons on nanostructured metal surfaces. *Phys Rev Lett* 95:116802.
33. Langhammer C, Yuan Z, Zori I, Kasemo B (2006) Plasmonic properties of supported pt and pd nanostructures. *Nano Lett* 6:833–838.
34. Johnson PB, Christy RW (1975) Optical constants of copper and nickel as a function of temperature. *Phys Rev B* 11:1315.
35. Wang H, Tam F, Grady NK, Halas NJ (2005) Cu nanoshells: Effects of interband transitions on the nanoparticle plasmon resonance. *J Phys Chem B* 109:18218–18222.
36. Schröster U, Heitmann D (1999) Grating couplers for surface plasmons excited on thin metal films in the kretschmann-raether configuration. *Phys Rev B* 60:4992–4999.
37. Pang L, Hwang GM, Slutsky B, Fainman Y (2007) Spectral sensitivity of two-dimensional nanohole array surface plasmon polariton resonance sensor. *Appl Phys Lett* 91:123112.
38. Sherry LJ, Jin R, Mirkin CA, Schatz GC, Duyne RPV (2006) Localized surface plasmon resonance spectroscopy of single silver triangular nanoprisms. *Nano Lett* 6:2060–2065.
39. Hicks EM, *et al.* (2005) Plasmonic properties of film over nanowell surface fabricated by nanosphere lithography. *J Phys Chem B* 109:22351–22358.
40. Pettersson LAA, Snyder PG (1995) Preparation and characterization of oxidized silver thin films. *Thin Solid Films* 270:69–72.
41. Langhammer C, Schwind M, Kasemo B, Zoric I (2008) Localized surface plasmon resonances in aluminum nanodisks. *Nano Lett* 8:1461–1471.
42. Kim JH, Ehrman SH, Germer TA (2004) Influence of particle oxide coating on light scattering by submicron metal particles on silicon wafers. *Appl Phys Lett* 84:1278–1280.
43. Lahav M, Vaskevich A, Rubinstein I (2004) Biological sensing using transmission surface plasmon resonance spectroscopy. *Langmuir* 20:7365–7367.
44. Rindzevicius T, *et al.* (2005) Plasmonic sensing characteristics of single nanometric holes. *Nano Lett* 5:2335–2339.
45. Leebeeck A, *et al.* (2007) On-chip surface-based detection with nanohole arrays. *Anal Chem* 79:4094–4100.
46. Kuriharaa K, Nakamurab K, Suzuki K (2002) Asymmetric spr sensor response curve-fitting equation for the accurate determination of spr resonance angle. *Sens Actuators B* 86:49–57.
47. Love JC, *et al.* (2003) Formation and structure of self-assembled monolayers of alkanethiolates on palladium. *J Am Chem Soc* 125:2597–2609.